Material: Ferritic Steel: F82H
Property: Strain Hardening Rate
Data: Experimental
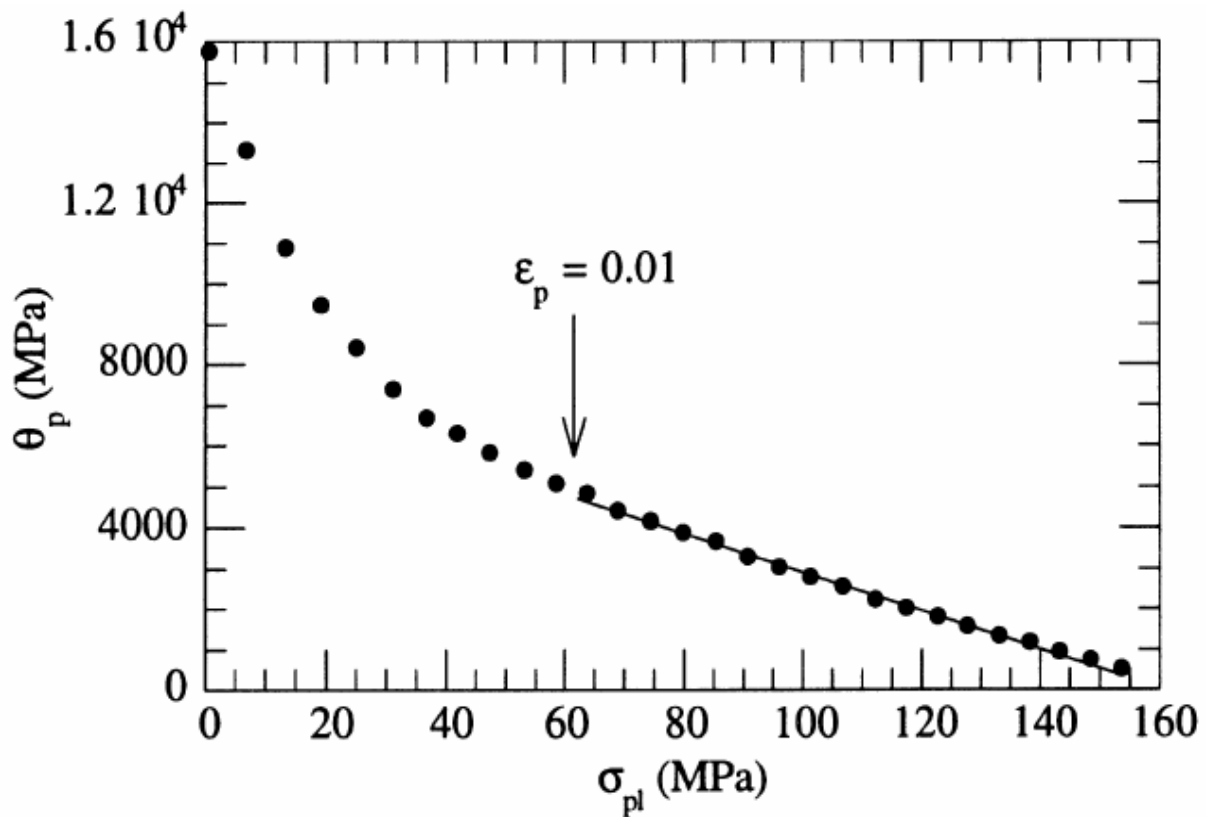

Fig. 1. Engineering stress–strain curve and strain-hardening rate θ_p versus σ_{pl} at $T = 293\,\mathrm{K}$ and $\dot{\varepsilon} = 2 \times 10^{-3}\,\mathrm{s}^{-1}$.
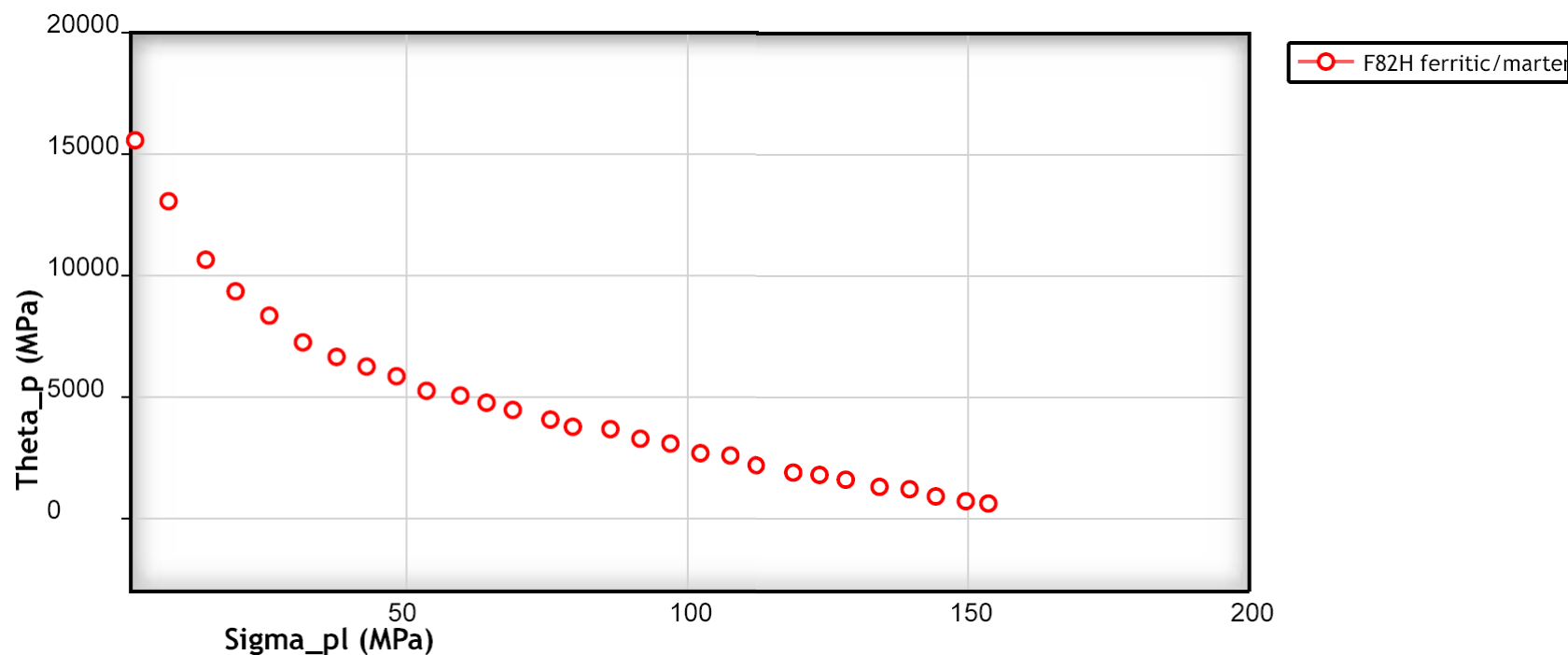
Title of paper (or report) this figure appeared in:
Constitutive behavior and fracture toughness properties of the F82H ferritic/martensitic steel

Author of paper or graph:
P. Spatig, G.R. Odette, E. Donahue, G.E. Lucas

Strain hardening rate theta_p versus sigma_pl at T=293K and epsilon = 2*10^-3 s^-1

View Data   Author Comments

Plot Format:
    Y-Scale: ⦿ linear ○ log ○ ln
    X-Scale: ⦿ linear ○ log ○ ln
    Update   Close Window

Constitutive behavior and fracture toughness properties of the F82H ferritic/martensitic steel

P. Spätig *, G.R. Odette, E. Donahue, G.E. Lucas

Department of Chemical Engineering, University of California, Santa Barbara, CA 93106-5080 USA

Abstract

A detailed investigation of the constitutive behavior of the International Energy Agency (IEA) program heat of 8 Cr unirradiated F82H ferritic–martensitic steel has been undertaken in the temperature range of 80–723 K. The overall tensile flow stress is decomposed into temperature-dependent and athermal yield stress contributions plus a mildly temperature-dependent strain-hardening component. The fitting forms are based on a phenomenological dislocation mechanics model. This formulation provides a more accurate and physically based representation of the flow stress as a function of the key variables of test temperature, strain and stain rate compared to simple power law treatments. Fracture toughness measurements from small compact tension specimens are also reported and analyzed in terms of a critical stress–critical area local fracture model. © 2000 Elsevier Science B.V. All rights reserved.

1. Introduction

The work described here is part of a broader effort to characterize both the constitutive and fracture behaviors of advanced ferritic–martensitic steels in support of developing physically based models for accurately predicting defect tolerance in flawed fusion structures, based in large part on small specimen test methods. This paper focuses on the International Energy Agency (IEA) heat of martensitic steel F82H and presents: (a) a new compact, multi-term constitutive equation, with a new approach of treating strain-hardening behavior; (b) recent cleavage fracture toughness–temperature data obtained with small compact tension specimens; and (c) analysis of the fracture data with a micromechanical model to derive local measures of cleavage toughness.

2. Experimental

The alloy in this study is the reduced activation F82H steel being investigated as part of an IEA coordinated program on ferritic/martensitic steels. The F82H steel contains 7.65 wt% Cr, 2 wt% W, and Mn, Mo, V, Ta, Ti, Si and C below 1 wt% in sum total, and Fe for the balance. The steel was heat treated by normalizing at 1313 K for 0.5 h and tempering at 1013 K for 2 h [1].

Tensile tests were performed on round specimens 3 mm in diameter and 18 mm in gauge length. The tests were carried out on a servo-hydraulic machine at constant nominal strain rates of 2×10^{-4} s^{-1}, 2×10^{-3} s^{-1} and 2×10^{-2} s^{-1} in the temperatures range from 80 to 293 K. In addition, previous tests at temperatures up to 723 K at nominal strain rates of 2.8×10^{-5} s^{-1} and 2.8×10^{-4} s^{-1}, performed at the Paul Scherrer Institute in Switzerland [2], are re-analyzed in this paper.

As a part of an extensive study of the effect of specimen geometry and size on fracture toughness, tests were carried out on fatigue pre-cracked, 20% side-grooved, 4.6 mm thick compact tension (0.18T CT) specimens, with crack length a to specimen width W ratios of $a/W \cong 0.5$ and a specimen thickness (B) to width ratio of $B/W = 0.5$. Static tests, at a ram displacement rate of about 4 µm/s, were carried out under displacement control on a servo-hydraulic load frame at temperatures

---

* Corresponding author. Present address: Ctr Recherches/ Physique des Plasmas, Ecole Polytechnique Fed de Lausanne, Fusion Technology Materials OVGA/2, 5232 Lausanne, Switzerland. Tel.: +41-56 310 20 63; fax: +41-56 310 45 29.

E-mail address: philippe.spatig@psi.ch (P. Spätig).

ranging from 77 to 188 K. Temperature control was provided by either a liquid-nitrogen-cooled alcohol bath or a regulated N_2 gas environment. Test and analysis procedures to determine K_{Jc} or K_q, representing valid small scale yielding elastic–plastic toughness and large scale yielding toughness, respectively, were based on ASTM Standard Practice E813 and E1921-97.

3. Results and discussion

3.1. Strain-hardening and constitutive behavior

Examples of true stress–true strain curves have previously been reported in [3]. The yield stress (σ_y) exhibits a strong temperature (T) and strain rate ($\dot{\varepsilon}$) dependence, σ_y ($T, \dot{\varepsilon}$), as expected for bcc alloys [4] The σ_y can be decomposed into athermal and thermal components. The low temperature thermal component, σ_{yt} ($T, \dot{\varepsilon}$), is controlled by the lattice friction, or Peierls, stress. Over a small range of intermediate temperatures, possibly other more weakly activated mechanisms, associated interstitial solutes, strengthened by the polycrystalline grains and dislocation intersections, can contribute. At higher temperatures that are still below the creep regime, an athermal component, σ_{ya}, depends on alloy composition and processing history mediated microstructure, and includes contributions from: (a) the initial dislocation density; (b) non-deforming particles such as carbides; (c) weaker precipitate phases; (d) substitutional solutes; and (e) polycrystalline grain and subgrain boundaries.

As proposed by Zerilli and Armstrong [5], the post yield flow stress, σ ($\varepsilon, \dot{\varepsilon}, T$), can be decomposed as the sum of yield stress and strain hardening, σ_{pl}, contributions: σ ($\varepsilon, \dot{\varepsilon}, T$) = σ_y ($T, \dot{\varepsilon}$) + σ_{pl} ($T, \varepsilon, \dot{\varepsilon}$), where ε is the true plastic strain. The σ_{pl} is experimentally defined as σ ($\varepsilon, \dot{\varepsilon}, T$) − σ_y ($T, \dot{\varepsilon}$). Strain hardening is primarily the consequence of dislocation multiplication and corresponding dislocation–dislocation interactions. Thus σ_{pl} is expected to be much less sensitive to T and $\dot{\varepsilon}$ than σ_y. For example, long-range stress field interactions are clearly athermal. Indeed, qualitatively similar strain hardening was found at all temperatures and strain rates investigated in this study. However, strain-induced dislocation structures re-organize into lower energy configurations by forming cell substructures as well as through mutual annihilation. At low temperatures strengthening by interactions of screw dislocations is also thermally activated [6]. Finally, dislocation multiplication is expected to depend on the character of the mobile dislocations and operative dislocation sources. Hence, σ_{pl} is not expected to be completely athermal nor to depend monotonically on temperature. Further, the dislocation re-structuring suggests that, rather than a simple power law behavior, the constitutive model should allow for a decreasing rate of strain hardening,

perhaps ultimately saturating at high strains, as suggested by Voce [7].

Mecking [8] proposed a convenient and systematic way to analyze strain hardening data by plotting a hardening rate parameter, $\theta_p = \mathrm{d}\sigma_{pl}/\mathrm{d}\varepsilon_p$, as a function of σ_{pl}. As shown in Fig. 1 for a test at $\dot{\varepsilon} = 2 \times 10^{-3}\,\mathrm{s}^{-1}$ and 293 K, θ_p systematically decreases with increasing σ_{pl}. Above about $\varepsilon_p = 0.01$, the θ (σ_{pl}) curve is approximately linear, extrapolating to $\theta_p = 0$ (saturation) at $\sigma_{pl} \cong 160$ MPa. The strain-hardening behavior was similar for all test conditions in this study. Thus, for $\varepsilon_p \geqslant 0.01$ the θ_p data can represented as

$$\theta_p = \frac{\mathrm{d}\sigma_{pl}}{\mathrm{d}\varepsilon_p} = K_1 - K_2\sigma_{pl}, \qquad (1)$$

where K_1 (MPa) and K_2 (dimensionless) are fit parameters that may depend on temperature and strain rate. Integration of Eq. (1), with the initial condition $\sigma_{pl} = \sigma_{0.01} = \sigma_{pl}$ ($\varepsilon_p = 0.01$), yields

$$\sigma_{pl}\ (\varepsilon_p) = \sigma_{sat} - \frac{K_1}{K_2}\exp\left[-K_2[\varepsilon_p - 0.01]\right]. \qquad (2)$$

Here the saturation stress, σ_{sat}, is equal to $K_1/K_2 + \sigma_{pl}(0.01)$. Of course, σ_{sat} cannot be reached in a tensile test due to necking. Additional deformation tests
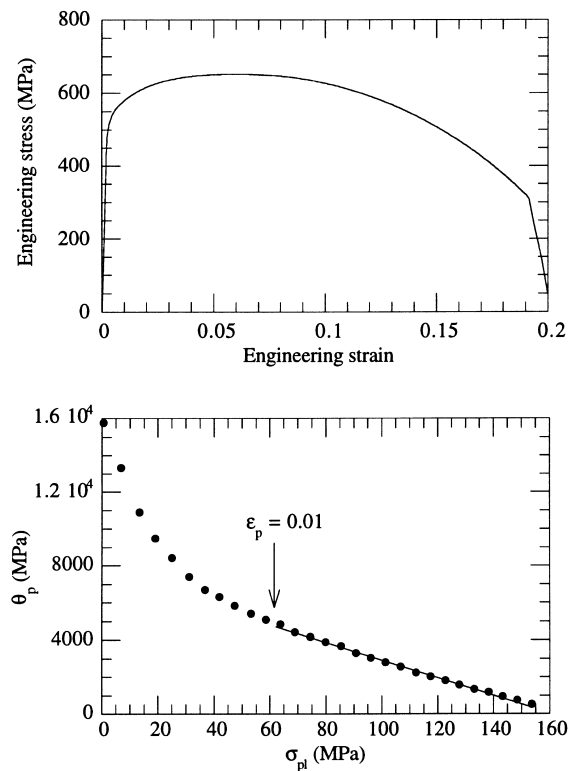

Fig. 1. Engineering stress–strain curve and strain-hardening rate θ_p versus σ_{pl} at $T = 293\,\mathrm{K}$ and $\dot{\varepsilon} = 2 \times 10^{-3}\,\mathrm{s}^{-1}$.

in other configurations will be required to verify the saturation behavior and magnitude. As noted above, a mechanistic justification for this exponential type of stress–strain relation was originally proposed by Voce [7]. More importantly, the classical strain-hardening law for engineering materials of the type $\sigma = K\varepsilon_p^n$ is not compatible with a linear decrease of θ_p or a saturating σ_{pl}. Further, in this case, n implicitly depends on σ_y; and higher σ_y at lower temperature, or higher strain rates, results in a lower apparent n, even if the actual strain-hardening behavior is completely athermal.

Any temperature and strain rate dependence of σ_{pl} are represented by the empirical K_1, K_2 and σ_{sat} terms. Following Kocks [9], Fig. 2 plots the logarithm of non-dimensional σ_{sat}/μ and $(K_1/K_2)/\mu$ as well as K_2, versus the dimensionless temperature, $x = 100 \, kT/\mu b^3$. Here μ is the shear modulus, $\mu = E/2(1+v)$, v is Poisson's ratio, E is Young's modulus given by [10]

$$E(\text{MPa}) = 6900 \times (32.3 - 6.16 \times 10^{-3}T - 4.34 \times 10^{-6}T^2)$$
$$(T \text{ in K})$$

and b is the Burgers vector ($= 0.268$ nm). The logarithms of both σ_{sat}/μ and $(K_1/K_2)/\mu$ decrease roughly linearly between $x = 100kT/\mu b^3$ values of about 0.2 to 0.75, corresponding to about 220 to 720 K. The K_2 increases roughly linearly between about $x = 0.2$ and 0.65, corresponding to about 220 to 640 K. Empirical least square fits to the strain hardening parameters from 220 to 640 K, shown as the solid lines in Fig. 2, are

$$(K_1/K_2)/\mu = 33.501 \times 10^{-4} \times (3.232 \times 10^{-2})^x, \tag{3a}$$

$$\sigma_{sat}/\mu = 33.174 \times 10^{-4} \times (1.705 \times 10^{-1})^x, \tag{3b}$$

$$K_2 = -4.1087 + 186.86 \times x. \tag{3c}$$

The effect of strain rate has been ignored in these fits, consistent with the data for the limited range of rates examined in this study and accepting a common fit to the high and low temperature data. The general validity of this assumption will require additional testing. The strain-hardening formulation represented by Eqs. (2)–(3c) emphasizes behavior over a broad range of temperatures above about 220 K. For lower temperatures $(K_1/K_2)\mu$ ($x < 0.2$) and K_2 ($x < 0.15$) are roughly constant, while σ_{sat}/μ decreases by about 25%. Using the parameters corresponding to 220 K overestimates σ and σ_{pl} at 80 K by an average of about 35 MPa (with a range of about 25–45 MPa) or less than 4% of the total flow stress. Separate fits (e.g., for $T < 300$ K) would be needed to provide more accurate treatment of the constitutive behavior at lower temperatures.

A strain-rate compensated temperature T' can be defined to correlate σ_{yt} $(T, \dot{\varepsilon})$ as $\sigma_{yt}[T'(\dot{\varepsilon})]$ [4,10]. The σ_{yt} at T for a strain rate $\dot{\varepsilon}$ corresponds to the same σ_{yt} at a
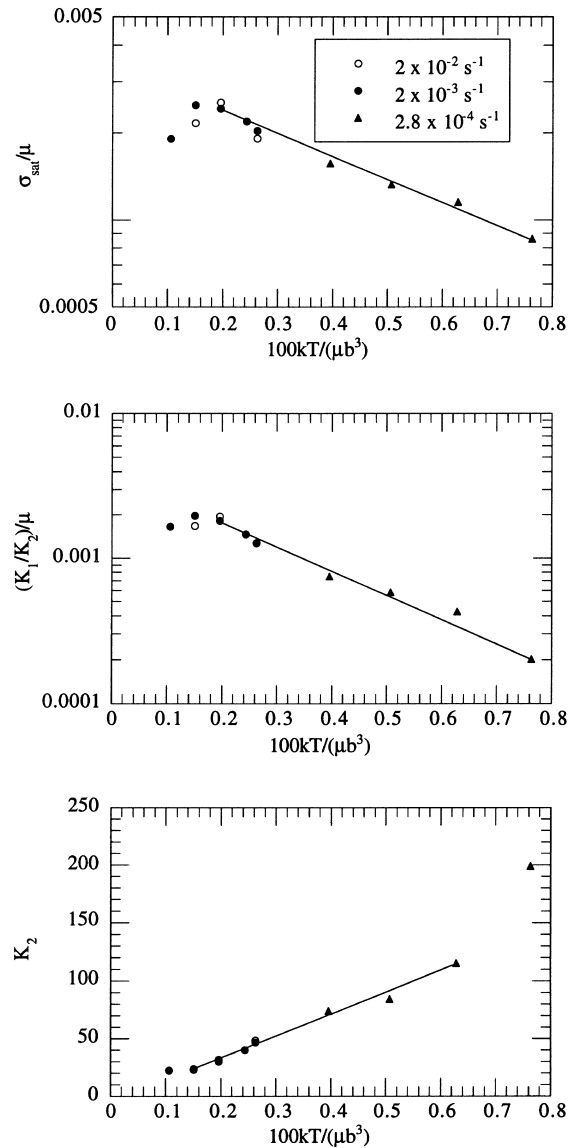

Fig. 2. Normalized strain-hardening parameters versus normalized temperature.

reference strain rate $\dot{\varepsilon}_r$ at T'. The relation between T', $\dot{\varepsilon}$ and T is given by

$$T' = T[1 + C \ln(\dot{\varepsilon}_r/\dot{\varepsilon})]. \tag{4}$$

The σ_{yt} $(T, \dot{\varepsilon})$ is experimentally defined as $\sigma_{yt}(T, \dot{\varepsilon}) = \sigma_y (T, \dot{\varepsilon}) - \sigma_{ya}(T)$ by fitting the weakly temperature dependent athermal contribution $\sigma_{ya}(T)/\mu(T) \cong$ constant. The σ_{yt} has two apparent regimes [4]. In regime I, below about 220 K, the Peierls mechanism is dominant [4]. In regime II, from about 220 to 300 K, σ_{yt} appears to be controlled by somewhat weaker thermally activated processes noted previously. Above about 300 K, $\sigma_{yt} \cong 0$.

The σ_y data in the low temperature regime I, including data from strain rate jump experiments [4], give a best fit value of $C \cong 0.042$, with the reference strain rate taken as $\dot{\varepsilon}_r = 2 \times 10^{-4}$ s^{-1}. This value of C is somewhat larger than reported previously [10], but broadly consistent with data in the literature ($\cong 0.03 - 0.05$) [11,12]. The overall $\sigma_y(T')/\mu$ can be correlated with a function of the form, $\sigma_y(T') = \sigma_{ya} + \sigma_{yt}(0)[1 - (T'/T_c)^{m_1}]^{m_2}$, where $\sigma_{ya}, \sigma_{yt}(0), T_c, m_1$ and m_2 are fit parameters [13]. The $\sigma_{yt}(0)$ in the second term is the maximum value of σ_{yt} at 0 K, T_c is the effective critical temperature when σ_{yt} goes to 0, and m_1 and m_2 are related to the form of the activation barrier. In practice, m_1 and m_2 parameters provide for curvature in the $\sigma_{yt}(T')$. The data in this study can be fit by

$$\sigma_y/\mu = 6.50 \times 10^{-3}, \qquad T' > 270 \text{ K}, \tag{5a}$$

$$\sigma_y/\mu = 6.50 \times 10^{-3} + 0.0123 \times [1 - (T'/270)^{0.9}]^2,$$
$$T' < 270 \text{ K}. \tag{5b}$$

The empirical m_1 and m_2 fit parameters yield a $\sigma_{yt}(T')$ shape that is very similar to that proposed by Dorn and Rajnak [14] based on a double kink nucleation model; indeed, the curves are virtually identical for a $T_c = 300$ K rather than 270 K.

Fig. 3 compares the predicted flow stress (Eqs. (3a)–(5b)), for strains up to necking to measured values for temperatures from 220 to 625 K, strain rates from 2×10^{-4} s^{-1} and 2×10^{-2} s^{-1} (as indicated by the various symbols). Each symbol type corresponds to a test at a given temperature and strain rate. Agreement is good with an S.E. and bias of about 9 and 12 MPa, respectively.

The most notable feature of these results is that this bcc alloy shows a strain-hardening behavior that is more fcc-like in character, even at low temperatures. In low dislocation density bcc single crystals, strain hardening and dislocation interaction mechanisms are dominated
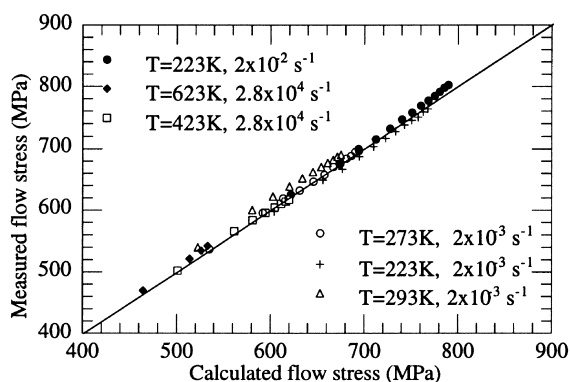
by the formation and collapse of junctions at the intersection of bowed edge segments of otherwise straight screw dislocations. In this regime, junction collapse is controlled by the rate of kink nucleation on straight screw segments [15]. This suggests that strain hardening should be dependent on both temperature and strain rate. However, such mechanisms are only dominant if the overall dislocation density is sufficiently low, and if edge segments are not effectively stored. While these processes may play a role, they clearly do not dominate in complex structural alloys, such as F82H, where nascent dislocation densities exceed 10^{14} m^{-2} [16] and complex pinning point and boundary structures result in complex mixed screw and edge substructures.

Kocks [9] rationalized Voce curves for fcc metals and alloys by developing a phenomenological model of strain hardening based on the storage and the dynamic annihilation of dislocations. The model predicts a linear relation between the strain hardening and the flow stress, similar to Eq. (2). K_1 is the term related to the storage rate of dislocations, depending on their mean free path, while K_2 characterizes the dynamic dislocation annihilation. It has been experimentally shown that dislocation storage and annihilation take place even at low temperatures in both fcc and bcc metals [17]. The annihilation of the screw segments can occur by cross-slip owing to the strong elastic interaction [18] between them, and the annihilation of non-screw segments can take place either by climb (only important at high temperature) or by spontaneous annihilation on the same glide plane or when the attractive elastic force between two dislocations on different glide plane exceeds the force required for dislocation climb [19,20]. Note that in the Kocks model the key structure parameter is the total dislocation density; the detailed distribution of dislocations and their evolution with strain are not treated. Given the complex structure of these steels, more detailed models than that of Kocks should be evaluated. In particular, the evolution of the dislocation structure within the laths and the prior austenite grain and lath boundaries are likely to play important roles. More advanced models have been developed to account for the evolution and reorganization of dislocation structures up to large strain, e.g. [21–24]. For example, the recent cell structure-based model of Fang and Dahl [23] yields a relation for the evolution of the dislocation density similar to that of Kocks by taking into account dislocation re-organization.

3.2. Fracture testing and analysis

Results of the fracture tests are shown in Fig. 4, where toughness $K_{Jc/q}$ data are plotted as a function of test temperature. The tests were performed in the lower shelf and transition region, where the typical and inherently large scatter was observed in the latter. All
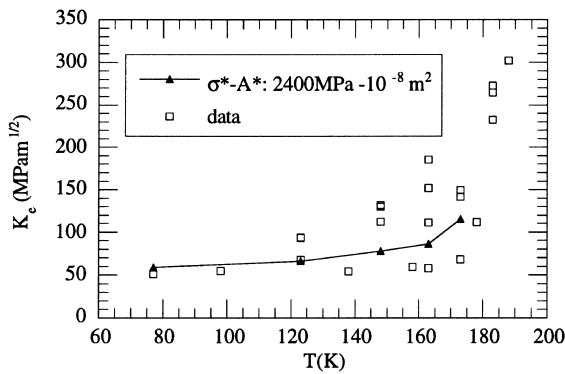

Fig. 3. Measured flow stress flow stress versus calculated flow stress for different temperatures and strain rates.

Fig. 4. Effective fracture toughness K_e for the 0.18T CT and critical stress–critical area model predictions.

specimens failed by quasi-cleavage, in some cases, following a large amount of plastic deformation and crack blunting, resulting in loss of constraint [25,26]. Constraint loss is primarily associated with plasticity encompassing a large fraction of the uncracked ligament of length, b. The degree of such in-plane constraint loss can be characterized by a non-dimensional constraint parameter $M = b\sigma_y E'/K_q^2$, where E' is the plane strain elastic modulus. As M decreases from large values, which may need to be well in excess of 100 to fully maintain small scale yielding conditions, K_q gradually increases. At low values of M, below about 30, massive constraint loss occurs, and K_q increases rapidly. The quantitative effects of constraint loss depend on the detailed micromechanics of fracture and the local fracture properties (see below). For the specimen geometry used here, values of M greater than about 60 are probably sufficient to ensure reasonably high constraint. Thus the maximum 'valid' K_{Jc} is estimated to be about 100 MPa m$^{1/2}$. At temperatures higher than 180 K, a clear lateral contraction of the specimens near the crack tip was observed, suggesting additional out-of-plane constraint loss. In this regime, both in-plane (controlled by b) and out of plane (controlled by B and side grooving) constraint rapidly diminishes.

The issues associated with constraint variations can be mitigated by assessing the local fracture properties that do not depend on the level of deformation. Defining local properties requires a micromechanical model of cleavage. The most common and empirically successful micromechanical model is that cleavage occurs when the critical tensile stress (σ^*) encompasses a critical area (A^*) ahead of the crack tip [26,27]. Thus $\sigma^* - A^*$ constitute the local fracture properties. The macroscopic toughness is the corresponding K_J that produces the critical stress fields required for cleavage, that are, up to some point, independent of conditions of constraint.

Two-dimensional simulations of crack tip stress (and strain) fields were performed with the ABAQUS™ 5.8

code assuming plane strain conditions for lateral constraint. ABAQUS models the effect of the multi-axial stress state using the Mises stress potential and associated J_2 flow law. These computations require a uniaxial constitutive equation, based on the test temperature ($T < 200$ K) and effective process zone strain rate. The constitutive equation described above was used with the strain hardening contribution set at 220 K for reasons discussed previously. Since the transition regime temperature is lower, use of σ_{pl} (220 K) is an approximation. However, this has little effect on the overall results and is equivalent to a small temperature shift of about -10 K in the curve. Values of $\sigma^* - A^*$ can be estimated by fitting the $K_{Jc/q}$ (T) to experimental data.

Results of the calculated $K_{Jc/q}$ (T) curve for the 0.18T CT specimens are presented in Fig. 4 for $\sigma^* = 2400$ MPa and $A^* = 0.8 \times 10^{-8}$ m^2, and agree well with the data trend. Note that these values of A^*, as well as the values of $K_{Jc/q}$, for the 0.18T CT specimens are slightly larger than that ($A^* = 0.8 \times 10^{-8}$ m^2) found for bend bar specimens with a similar W and b and $B/W = 1$ [26]. There are several possible explanations for these differences, including some combination of: (a) weakest link-type statistical effects associated with the crack front length which is roughly 2.8 larger for the 3PB compared to the CT specimens; (b) maintenance of greater lateral constraint for the bend specimens with a larger $B/W = 1$; (c) details of the side grooving; and (d) material variability. Further testing and analysis are planned to clarify this issue.

4. Summary

Tensile and fracture toughness tests have been performed on specimens from the IEA heat of F82H. A constitutive equation was developed from these data, based on a decomposition of the flow stress into thermally activated and athermal components of the yield stress plus a strain-hardening component that has a mild temperature dependence and a saturation level at high strains. The physical basis for the yield stress term has been discussed previously. The strain-hardening behavior is consistent with a model based on a temperature dependent competition between dislocation storage and annihilation. Additional deformation testing will be conducted to verify and refine the constitutive model.

Fracture toughness measurements of 0.18T CT specimens were performed in the lower transition region. The data were fit by a local critical stress–critical area model for cleavage initiation. It was found that the area parameter, as well as the effective toughness, of the 0.18T CT specimens are slightly higher than those previously found for similar sized bend bar but with $B/W = 1$. Once again, more testing and modeling will be required to resolve these differences.

Acknowledgements

References

[1] M. Tamura, H. Hayakawa, M. Tanimura, A. Hishinuma, T. Kondo, J. Nucl. Mater. 141–143 (1986) 1067.

[2] P. Spätig, R. Schäublin, S. Gyger, M. Victoria, J. Nucl. Mater. 258–263 (1998) 1345.

[3] P. Spätig, G.R. Odette, G.E. Lucas, M. Victoria, DOE Fusion Materials Semiannual Progress Report, DOE/ER-0313/26, 1999, p. 83.

[4] P. Spätig, G.R. Odette, G.E. Lucas, J. Nucl. Mater. 275 (1999) 324.

[5] F.J. Zerilli, R.W. Armstrong, J. Appl. Phys. 61 (1987) 1816.

[6] D. Kuhlmann-Wilsdorf, Philos. Mag. A 79 (4) (1999) 955.

[7] E. Voce, J. Inst. Met. 74 (1968) 537.

[8] H. Mecking, Work Hardening in Tension and Fatigue, in: A.W. Thompson (Ed.), Am. Inst. Min. Engrs., NY, 1977, p. 67.

[9] U.F. Kocks, ASME J. Eng. Mater. Technol. 98 (1976) 72.

[10] K. Edsinger, PhD thesis, University of California, Santa Barbara, 1995, p. 115.

[11] M. Cagnon, Philos. Mag. 24 (1971) 1465.

[12] J. Diehl, G.P. Seidel, M. Weller, Trans. JIM 9 (1968) 219.

[13] T. Wille, W. Gieseke, C. Schwink, Acta Metall. 35 (1987) 2679.

[14] J.E. Dorn, S. Rajnak, Trans. AIME 230 (1964) 1052.

[15] M. Tang, B. Devincre, L.P. Kubin, Model. Simul. Mater. Sci. Eng. 7 (5) (1999) 893.

[16] R. Schäublin, P. Spätig, M. Victoria, J. Nucl. Mater. 258–263 (1998) 1178.

[17] U. Essmann, H. Mughrabi, Philos. Mag. A 40 (6) (1979) 731.

[18] U. Essmann, Acta Metall. 12 (1964) 1468.

[19] J. Friedel, Dislocations, Pergamon, London, 1964.

[20] U. Essmann, M. Rapp, Acta Metall. 21 (1973) 1305.

[21] X.F. Fang, W. Dahl, Mater. Sci. Eng. A 203 (1995) 14.

[22] X.F. Fang, C.O. Gusek, W. Dahl, Mater. Sci. Eng. A 203 (1995) 26.

[23] X.F. Fang, W. Dahl, Mater. Sci. Eng. A 203 (1995) 36.

[24] Y. Estrin, L.S. Tóth, A. Molinari, Y. Bréchet, Acta Metall. 46 (15) (1998) 5509.

[25] H.J. Rathbun, G.R. Odette, M.Y. He, G.E. Lucas, J.W. Sheckherd, Pressure Vessels and Piping, Vol. 393, Fracture, Fatigue and Weld Residual Stress, ASME 1999, p. 17.

[26] G.R. Odette, K. Edsinger, G.E. Lucas, E. Donahue, ASTM-STP-1328, American Societyfor Testing and Materials, Philadelphia, PA (1998) p. 298.

[27] G.R. Odette, G.E. Lucas, J. Nondestr. Evalu. 15 (3/4) (1996) 137.